# Assessment of morphometry of pulmonary acini in mouse lungs by nondestructive imaging using multiscale microcomputed tomography

Dragoş M. Vasilescu[a,b], Zhiyun Gao[a,c], Punam K. Saha[a,c], Leilei Yin[d], Ge Wang[e], Beatrice Haefeli-Bleuer[f], Matthias Ochs[g], Ewald R. Weibel[f,1], and Eric A. Hoffman[a,h,i,1]

[a]Department of Radiology, University of Iowa, Iowa City, IA 52242; [b]Department of Diagnostic Radiology, Philipps University, 35032 Marburg, Germany; [c]Department of Electrical Engineering, University of Iowa, Iowa City, IA 52242; [d]Beckman Institute, University of Illinois, Urbana, IL 61801; [e]Biomedical Engineering and Sciences, Virginia Tech, Blacksburg, VA 24061; [f]Institute of Anatomy, University of Bern, Bern 9, Switzerland; [g]Institute of Functional and Applied Anatomy, Hannover Medical School, 30625 Hannover, Germany ; and Departments of [h]Medicine and [i]Biomedical Engineering, University of Iowa, Iowa City, IA 52242

Establishing the 3D architecture and morphometry of the intact pulmonary acinus is an essential step toward a more complete understanding of the relationship of lung structure and function. We combined a special fixation method with a unique volumetric nondestructive imaging technique and image processing tools to separate individual acini in the mouse lung. Interior scans of the parenchyma at a resolution of 2 μm enabled the reconstruction and quantitative study of whole acini by image analysis and stereologic methods, yielding data characterizing the 3D morphometry of the pulmonary acinus. The 3D reconstructions compared well with the architecture of silicon rubber casts of mouse acini. The image-based segmentation of individual acini allowed the computation of acinar volume and surface area, as well as estimation of the number of alveoli per acinus using stereologic methods. The acinar morphometry of male C57BL/6 mice age 12 wk and 91 wk was compared. Significant increases in all parameters as a function of age suggest a continuous change of the lung morphometry, with an increase in alveoli beyond what has been previously viewed as the maturation phase of the animals. Our image analysis methods open up opportunities for defining and quantitatively assessing the acinar structure in healthy and diseased lungs. The methods applied here to mice can be adjusted for the study of similarly prepared human lungs.

In the interest of efficient ventilation, the very large alveolar surface area of mammalian lungs is partitioned into small ventilatory units known as pulmonary acini, a sequence of branched ducts associated with gas-exchanging alveoli and connected to terminals of the conducting airway tree. In lung diseases such as emphysema, structural changes of the acini have a complex impact on lung function, entailing a loss of alveolar surface area associated with impaired structure of the centriacinar respiratory bronchioles that govern ventilation of the pulmonary acini (1). Therefore, quantifying such pathological changes at the acinar level is critical for understanding disease processes and their functional impact.

The acinus is the respiratory unit of the lung in which all alveoli are ventilated by the same transitional bronchiole (TB) that follows on terminal bronchioles (2, 3). The tubular alveolar duct system forms a branching tree that ends in the alveolar sacs, the cul-de-sac terminal generation of the airways. This architecture is functionally important, allowing the alveoli arranged along the duct system to be ventilated in series, which may result in a gradient in alveolar $O_2$ partial pressure (4, 5), a feature that could be enhanced by pathological changes. The analysis of this architecture demands the study of the 3D arrangement of structures, which is difficult to achieve by histological methods because it requires serial section reconstructions (6). To overcome these problems, Haefeli-Bleuer et al. (2) and Rodriguez et al. (3) have studied the acinar architecture of different species, including humans, by casting the lung with silicon rubber and then analyzing and measuring the branching pattern by microscopic dissections. This technique reaches a limit in very small lungs, such as in mice, and it does not permit direct quantitative assessment of the fine structure of the gas exchanger. These problems can be overcome by imaging techniques that allow a nondestructive analysis of lung fine structure (7). High-resolution (HRES) computed tomography (CT) combines the ability to study fine structures with the 3D reconstruction of architecture from serial sections while keeping the lung intact. In the present study, we explored the possibility of using this technique as an alternative approach to assessing the size and inner architecture of the mouse pulmonary acinus with morphometric techniques. We previously reported a method for fixing the lung in situ, maintaining an in vivo-equivalent lung architecture and providing a final ex vivo lung preparation whereby the air spaces remain air-filled (a requirement for subsequent X-ray–based imaging, as well as for representing physiological conditions) (7).

In this study, we examined the ability to nondestructively image the mouse lung using localized X-ray CT methods to capture images with 2-μm voxel dimensions (isotropic), along with the ability to process the resultant images to visualize and quantitate acinar-level geometry. We explored these methodologies by evaluating the lungs of C57BL/6 mice and comparing resultant images with those previously captured by casting methodologies in an independent study on BALB/C mice.

## Results

**Automatic Segmentation of Mouse Acinus.** A framework based on a multiscale topomorphologic opening approach (8) was developed to assist in segmenting individual acini from the acquired HRES images (Fig. 1). Multiscale fusions at the level of the septal walls at various locations caused by such factors as imaging artifacts, noise, and high variation in gray level intensities of the septal walls and pores of Kohn present challenges to simple segmentation algorithms. Saha et al. (8) developed a method using the multiscale morphologic signature of individual objects at conjoining locations that requires no previous knowledge of
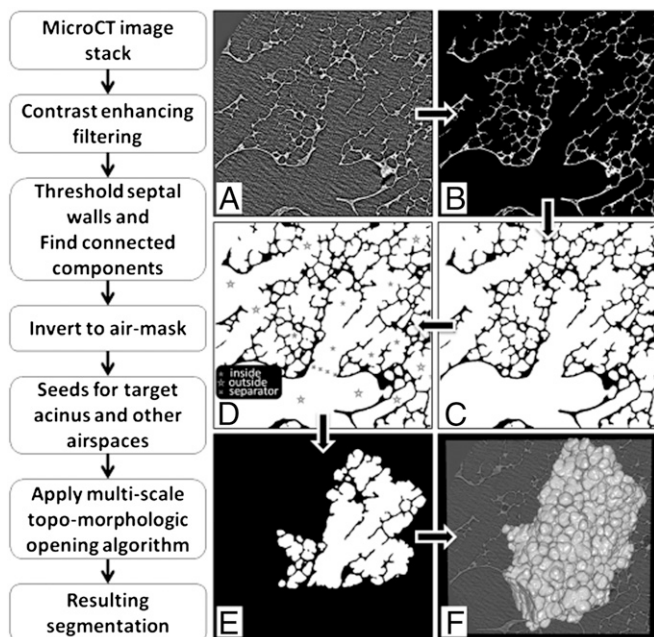
PHYSIOLOGY

**Fig. 1.** Flowchart of acinar segmentation in HRES images. Sample images for the main steps of the acinar segmentation procedure. (*A*) Initial contrast enhancement using unsharp mask filtering. (*B*) Result of thresholding and connected component finding. (*C*) Inverted and smoothed mask. (*D*) Seed points inside and outside the acinus of interest. (*E*) Remaining acinar mask. (*F*) 3D surface rendering of the segmented acinus with original orthogonal image slice.

constraints on geometric, shape, or image intensity models for individual objects.

We developed an image processing protocol with an effective graphical user interface that facilitates individual acinar segmentation using a multiscale topomorphologic opening algorithm (*Methods*). The HRES images cover a large volume and may contain multiple acini. After a threshold is chosen manually, a seed point is selected on the wall structure, and a connected component algorithm eliminates any structures not connected to the walls, with the assumption that all alveolar septa are interconnected, such as in a complex web.

In the present study, the separation of one individual acinus from neighboring air spaces required further user interaction (Fig. 1). Manual seed points had to be set to ensure correct separation (Fig. 1*D*). As a first step, the entrance to the acinus was identified by following the conducting airways to the point at which the first alveolus appeared, denoting the first-order respiratory bronchiole (Fig. 2). Multiple separator seed points were then set to separate the air space within the acinus from that in the conducting (terminal) airway (Fig. 1*D*).

Only two additional types of seeds were defined as inside and outside the object (acinus). Because of the complexity of the structure, an average of 40 seed points was required for a successful separation. Separators (i.e., seed points indicating the contact surface between structures that required separation) were required only at the entrance of the acinus and at locations where large, evidently incorrect wall interruptions were present. The air mask together with the seed points were used as the input parameters of the separation algorithm implemented for this application (8). In cases where the initial separation was incomplete, a second run had to be performed. For this, the exterior air spaces had to be deleted and new seed points were required on the remaining acinar structure. Movie S1 shows the reconstruction of a group of three acini on serial sections.

A similar procedure was used to identify pulmonary arteries and veins that supply blood to the acinus. To determine which vessel was transporting the venous blood and which vessel was transporting the reoxygenated blood, the larger vessels were tracked back to the heart in the large field-of-view scan.

Fig. 3 and Movie S2 show a 3D representation of three acini attached to their terminal bronchiole (TB), together with the vasculature transporting the blood to and from the area. The acini were segmented from the HRES images and visualized using ITK-Snap (9) (*Methods*); the vasculature was segmented and separated into arteries (blue) and veins (red) (Fig. 3*E*). Note that the pulmonary artery branch courses along the conducting airway, penetrating into the acinus from central regions, whereas the pulmonary veins approach the acini from the periphery. The volumetric segmentation of the acinus is the basis of the acinar analysis; thus, special attention must be given to proper segmentation. With the optimized segmentation algorithm, few manual corrections of the acinar mask were needed.

**Comparison of Reconstructed Acini with Silicon Rubber Casts.** A total of 22 pulmonary acini were imaged and reconstructed, 10 from young mice (age 12 wk) and 12 from old mice (age 91 wk). Fig. 4 shows two isolated acinar reconstructions viewed from the TB and from the side, compared with scanning electron micrographs of casts of two mouse acini of similar size. Here the reconstructed acini appear as compact structures; in contrast, the silicon rubber casts are spread out to some extent when mounted on the scanning electron microscope platform to show the branched nature of the acinar duct system, and thus may appear larger on this aspect. In the reconstructed acini, the alveoli appear as smooth ellipsoidal surfaces with no corners. The structure reconstructed is the alveolar surface in a perfusion-fixed air-filled lung, where the surface forces smooth the tissue surface (10). The alveoli in the silicon rubber cast appear smaller and less densely packed, because the casting material might not have removed all of the fluid in the alveoli (Fig. 4 *E* and *F*).

The smaller of the reconstructed acini (Fig. 4 *A* and *B*) was derived from one of the lungs of young mice, and the larger one (Fig. 4 *C* and *D*) was derived from a lung of old mice; their size corresponded to mean acinar size by age group (Table 1). The inflation level corresponded to approximately 60% of total lung capacity (TLC); this held for the silicon rubber casts as well. Acin size varied considerably. In the casting study, more than 600 acini were isolated by dissection along the airway tree from three lungs with a total volume of 0.7–1 mL, amounting to an inflation of approximately 60% of TLC, similar to that in the lungs studied by CT. The size distribution was approximately lognormal,
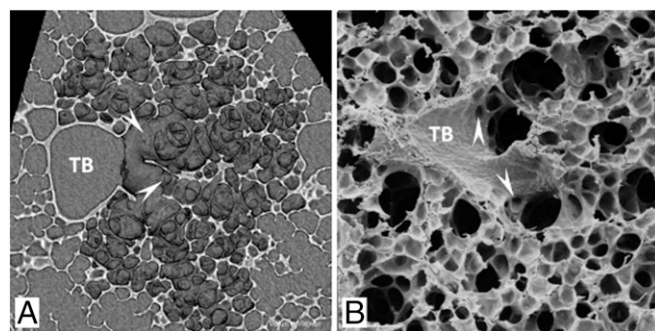


**Fig. 2.** Means of verifying the correct separation into individual acini at a terminal bronchiole based on the definition of acini starting at the first occurrence of alveoli on a TB (arrowheads). (*A*) HRES CT section with partial 3D simulation of a surface scan in which two acini were identified to branch off the TB in a C57BL/6 mouse. (*B*) Scanning electron micrograph of a perfusion-fixed Balb/C lung with two acini splitting from a TB.

Vasilescu et al.

www.manaraa.com
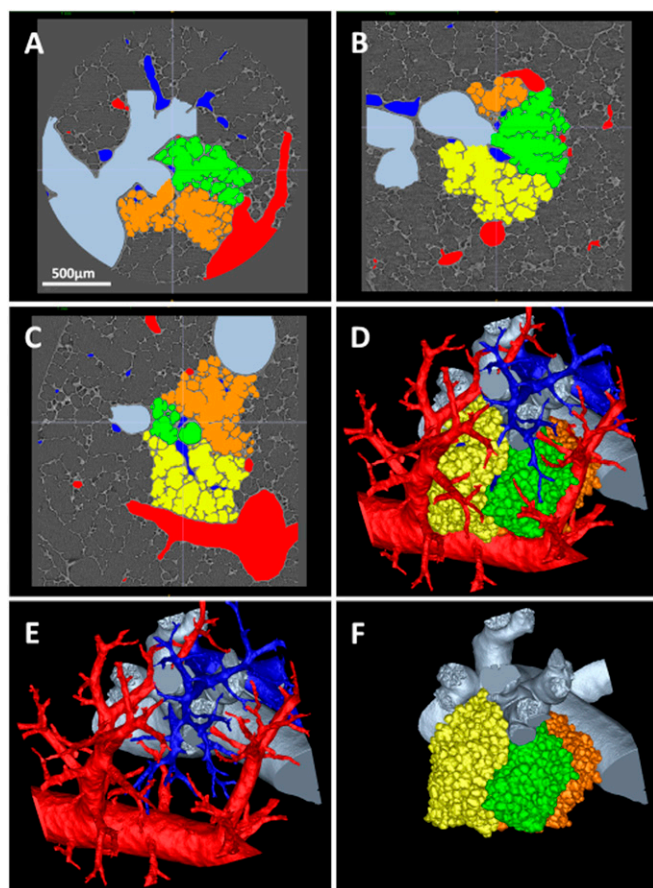
**Fig. 3.** Adjacent acini, TB, and supplying vasculature. (A–C) Orthogonal views (transxial, sagittal, and coronal) of the images at 2 μm with overlays of the segmented structures. (D) The 3D rendering of all segmented components. (E) TB with artery (blue) and vein (red). (F) TB supplying the three individual acini. Dynamic representations of the reconstruction process are shown in Movies S1 and S2.

ranging from 0.02 to 0.8 mm$^3$ (average, 0.1 mm$^3$) (Fig. 5). The volumes of the acini sampled and reconstructed in this study (Table S1) are also plotted in Fig. 5; the volumes of acini from the young mice fell in the same range, whereas the volumes of acini sampled from the older mice were larger, corresponding to the greater lung volumes (Table 1).

**Relationships Among Acinar Volume, Surface Area, and Number of Alveoli in Reconstructed Acini.** An advantage of the CT reconstruction approach is that it allows for the study of the internal fine structure of the individual acini on CT sections. In particular, stereologic methods can be applied to accurately assess the number of alveoli and the alveolar surface area per individual acinus by obtaining the required measurements or counts on a set of sections within the bounds of the acinus, as determined by the reconstruction procedure (Fig. 6 and Movie S1). The measurements thus obtained on the individual acini are given in Table S1. The mean total lung volume was significantly higher in the old mice compared with the young mice (mean, 1,398 ± 229 mm$^3$ vs. 959 ± 187 mm$^3$; $P = 0.001$) (Table 1), possibly due in part to the greater compliance in older mice (7, 11). Acinar volume was also significantly greater in the old mice (0.36 ± 0.15 mm$^3$ vs. 0.18 0.08 ± mm$^3$; $P = 0.002$). Two characteristics of lung morphometry can be deduced from these parameters: the relationship between acinar volume and body mass and the estimated number of acini per lung. The acinar

volume per body mass was higher in the old mice (0.011 mL/g vs. 0.006 mL/g). By dividing the average total lung volume by the average acinar volume for each age group, we estimated the number of the acini per lung at 5,328 acini in young mice and 3,883 in old mice, so that the lungs of older mice appear to contain fewer acini.

In accordance with the larger acinar volume, the alveolar surface area of the average acinus differed significantly (9.33 ± 4.15 mm$^2$ in the young mice vs. 16.81 ± 5.89 mm$^2$ in the old mice; $P = 0.003$), suggesting that the larger volume is not related solely to higher compliance. In contrast, the surface-to-volume ratio showed no significant difference between the age groups (52.00 ± 3.65 mm$^{-1}$ for the young mice vs. 47.73 ± 6.01 mm$^{-1}$ for the old mice), suggesting no difference in the geometry of the alveolar ducts with their alveolar sleeve.

The mean number of alveoli per acinus was 596 ± 326 in the young mice and 936 ± 254 in the old mice. The statistical analysis demonstrated a significant increase in alveoli in the old mice. In accordance with the finding of similar alveolar surface-to-volume ratio, the alveolar number per unit volume was not significantly different in the 2 groups. The general conclusion is that in the
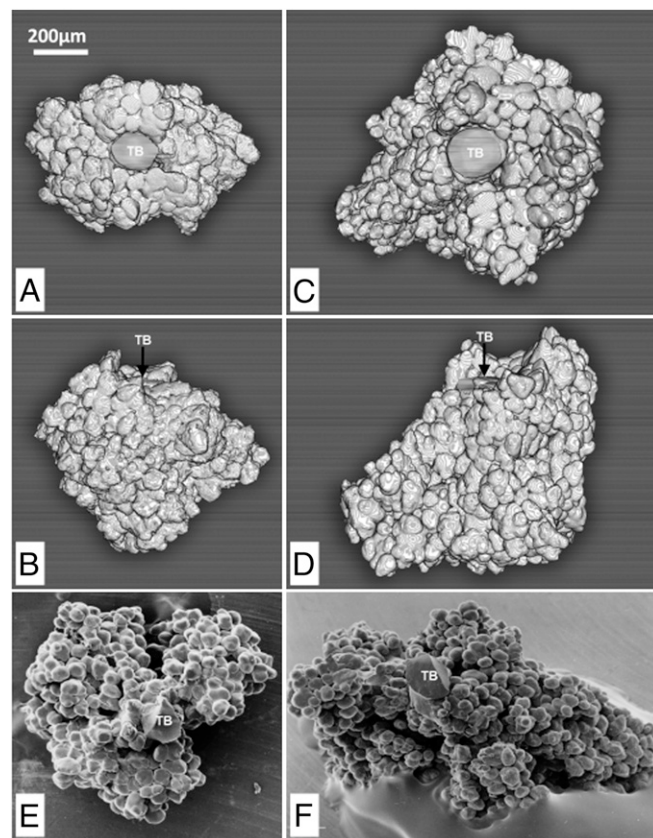


**Fig. 4.** Comparison of 3D volumetric renderings of acinar segmentations in young (12 wk) mice (A and B) and old (91 wk) mice (C and D) (both C57BL/6) with two representative acinar casts (Balb/C young mature mouse) (E and F). The 3D renderings are displayed in a top view (A and C) as well as in a side view (B and D). In E and F, the casts were imaged with a scanning electron microscope and spread out on the supporter to allow visualization of their architecture. The 3D renderings show the acini in their natural shape and state at an inflation pressure of ~60–70% of TLC. The acini of the C57BL/6 mice correspond in size to the average size of each age group (young, 0.15 mm$^3$; old, 0.38 mm$^3$). The silicon rubber casts correspond to an inflation of ~60% of TLC, with volumes of 0.11 mm$^3$ (E) and 0.24 mm$^3$ (F).

Vasilescu et al.

**Table 1. Morphometry of pulmonary acini in young mice (12 wk) and old mice (91 wk)**

| Parameter | Young mice | Old mice | P value |
|---|---|---|---|
| Body weight, g | 27.25 ± 1.26 | 31.67 ± 3.08 | 0.028* |
| Lung volume, mm$^3$ | 924 ± 154 | 1398 ± 139 | 0.001* |
| Acinus volume, mm$^3$ | 0.18 ± 0.08 | 0.36 ± 0.15 | 0.002* |
| Acinus surface area, mm$^2$ | 9.33 ± 4.15 | 16.81 ± 5.89 | 0.003* |
| Surface-to-volume ratio, mm$^{-1}$ | 52.00 ± 3.65 | 47.73 ± 6.01 | 0.064 |
| Alveolar number density, mm$^{-3}$ | 3071 ± 740 | 2591 ± 602 | 0.109 |
| No. of alveoli | 561 ± 307 | 881 ± 263 | 0.016* |

Morphometric characteristics of pulmonary acini comprise acinar volume, alveolar surface area in acinus, surface-to-volume ratio, and number of alveoli per acinus and per unit volume. Data are mean ± SD of a sample of 10 acini in four young mice and 12 acini in six old mice. Detailed data for individual acini are provided in Table S1.
*Significant differences identified by the t test between young and old.

larger lungs of the older mice, the acini are larger in terms of both mean volume and alveolar number and surface area.

## Discussion

The quantitative assessment of the structural basis of pulmonary gas exchange has traditionally been based on two independent approaches: (*i*) histological studies by light and electron microscopy on suitably sampled small tissue sections to determine, by means of stereologic methods, the quantitative parameters of the gas exchanger, such as surface area, volume, and number of alveoli and capillaries expressed per unit of lung volume and per total lung (12), and (*ii*) casting techniques to demonstrate the architecture and the connectivity of the airway and vascular system from the conducting airways (13) to the alveolar duct system of the acini (14). The latter approach permits the quantitative characterization of the size of acini, ventilatory units of the gas exchanger, and branching pattern and dimensions of the peripheral airway unit where the ventilation of the serially

arranged alveoli is combined with $O_2$ uptake by the capillaries (4), but it does not allow direct assessment of the functionally important parameters of these units, such as the acinar alveolar surface or the number of alveoli. The latter can be achieved in part by serial section reconstruction (6), but this approach has only limited potential, because the laborious reconstruction techniques do not allow analysis of adequate samples.

The foregoing problems can be overcome by HRES CT techniques, which generate a dense stack of precisely registered serial sections. Suitable algorithms, as described in this paper, can be used to segment individual acini by analyzing acinar airway connectivity and their relationship to the peripheral vascular system, corresponding to measurements with the casting technique. In a second step, the fact that the procedure has not destroyed the tissue structure allows us to study the internal fine structure of individual acini by applying stereologic methods to a sample of the sections to accurately estimate alveolar number and surface area within the bounds of the individual acinus as determined by the reconstruction procedure.

The unique capability to nondestructively image and segment individual whole acini in the ultra-HRES datasets opens up an opportunity to study the 3D morphometry in such a way as to provide the geometries needed in, for example, computational fluid dynamics (15–19), allowing for improved understanding of gas exchange and particle delivery to the lung periphery. The imaging and image analysis methods described here provide for branch morphometry at the acinar level that has not been available previously.

In this study, the lungs of young and old mice were compared. The volume, surface area, and number of alveoli in the acini were significantly higher in the old mice. At the same time, the surface-to-volume ratio and alveolar density were not significantly different between the 2 groups, but a possible decrease in the number of acini per whole lung was noted in old mice. These findings raise multiple questions that remain to be addressed.

This paper focuses on the characterization of acini as structural-functional entities, which mandates some caution when interpreting the results with respect to the whole lung. The approach used to obtain a sample of acini yields reliable estimates of some basic morphometric estimates, such as surface-to-volume ratio and alveolar number density, but it cannot yield a sample that meets all of the stereologic accuracy requirements for obtaining overall parameters characterizing the whole lung (12), such as total alveolar number and alveolar surface area. A different unbiased sampling approach in relation to the whole lung is required, and this has been done in separate studies on the same specimens (in preparation).

The total lung volume was 66% greater in the old mice compared with the young mice, but with only a 50% increase in acinar volume. This might suggest a loss in acini with aging. However, the increase in acinar volume is accompanied by an increased number of alveoli per acinus in the older mice, as well as an increase in acinar alveolar surface area. Thus, we must raise the question of whether this reflects not a loss of acini, but rather a partial fusion of acini that emanate from the same terminal bronchiole. Given recent observations suggesting that alveolar destruction may be preceded by peripheral bronchial obliteration in the development of emphysema (1), an understanding of ongoing normal and pathological structural changes in the peripheral lung is critical to an understanding of disease etiology. This will need further clarification in future studies.

In conclusion, the complex structure of the acinus is best understood when visualized in 3D. With current computer technology, it is now possible to generate 3D renderings of a segmentation that allows the viewer to freely rotate the acinus and use zooming for a more detailed or less detailed view. The segmentations can serve as the basis of volume measurements and surface area computations. Furthermore, estimation of the number of alveoli
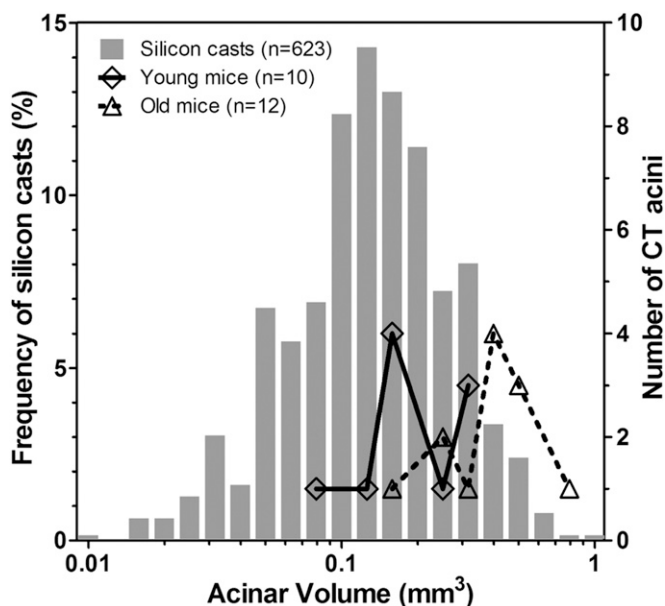


**Fig. 5.** Frequency distribution of acinar volume (in mm$^3$) for three groups of mice. The bars show the volume distribution of silicon rubber casts of acini in the young Balb/C mice. The overlaid data points represent the distribution of acini in the young and old C57BL/6 mice. Acinar size matches the silicon rubber casts for the young mice and is larger in the old mice.

Vasilescu et al.
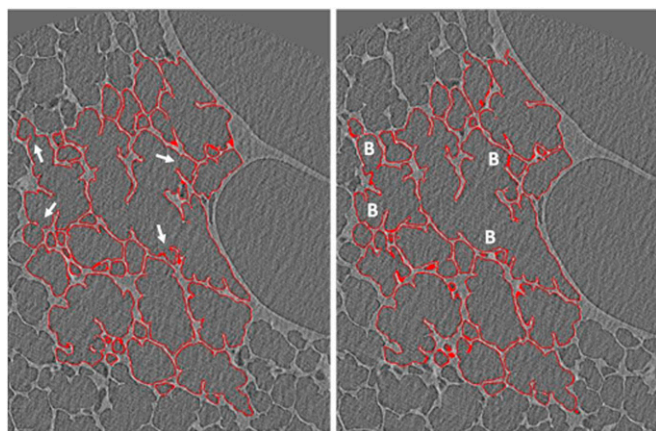
**Fig. 6.** Example of counting alveoli in the disector slice pairs by the appearance of alveolar entrance rings in form of bridges (B), where gaps of septal walls are present in the other section, as indicated by arrows. Counting is limited to the area of the acinus marked by the red outline of the alveolar surface area, resulting in number of alveoli per acinus (*Methods*).

within an acinus is possible by delineating a single acinus in the disectors based on 2D sections. The older mice demonstrated a significant increase in the number of alveoli, in both the whole lung and the average acinus. Furthermore, the data show a good correlation between acinar surface area and volume that increases with age nearly linearly. Thus, the significant increase in the number of alveoli supports the assumption of continued alveolarization after age 12 wk. These findings differ from the notion promulgated by Amy et al. (20) that all alveoli are formed by the 14th day after birth in Swiss–Webster albino mice. Caution is needed when comparing studies done on different mouse strains, however, given the differing airway morphometry in such mouse strains as C57BL/6, A/J, and Balb/C (21), which mandates the development and use of strain-specific atlases for evaluating pathological changes. The approach presented here has the potential to efficiently and accurately provide the data needed for such efforts.

## Methods

The experiments presented here were part of a larger study directed at creating an imaging-based comprehensive database/atlas describing the normal structure and physiology of the mouse lung. Fixed whole lung specimens were used to visualize the alveolar structures with a multi-resolution micro-CT scanner. The lung fixation method has been described by Vasilescu et al. (7).

For this study, two groups of male mice were used (all C57BL/6J; Jackson Laboratory): four mice aged 12 wk and six mice aged 91 wk, with average body mass of $27.25 \pm 1.26$ g and $31.67 \pm 3.08$ g, respectively. The animals were housed in an animal facility at the University of Iowa and provided with food and water ad libitum. All experimental protocols were approved by the University of Iowa's Institutional Animal Care and Use Committee.

**Imaging.** Imaging was performed on a MicroXCT-400 scanner (Xradia), with isotropic voxel dimensions ranging from 50 to 0.8 μm. Initial scans containing the whole lung (12–17 μm/voxel) allowed selection of coordinates for subsequent interior HRES scans (2 μm/voxel) without the need to section the lung into smaller blocks. The resolution of the whole lung scans allowed an approximation of the coordinates in the center of an acinus, because the rough outline of the acini was recognizable in the images. This imaging protocol allowed preservation of the spatial information, thereby enabling the linkage of HRES images to observations made on images of the whole lung at lower resolutions. The HRES imaging covered a field of view of 2 × 2 × 2 mm, thus including multiple acini, airways, and blood vessels. Two HRES scans were performed in each lung centered on acini, one in the upper left lung and the other close to the base of the caudal lobe. In cases where multiple acini were included in the field of view, all acini were segmented and

analyzed. The same imaging protocol as in a previous study (7) was used in this study for imaging the whole lung and the HRES scans.

**Automatic Segmentation of the Mouse Acinus.** Image segmentation was performed by implementing a framework that uses a multiscale topo-morphologic opening approach (8). This framework was developed to aid in segmenting individual acini from the acquired HRES images on a desktop PC (Dell T3500, eight-core hyperthreaded Intel Xeon CPU with 24 GB of RAM). Multiscale fusions at the level of the septal walls at various locations caused by such factors as imaging artifacts, noise, and high variation in gray-level intensities of the septal walls and pores of Kohn present challenges to simple segmentation algorithms such as thresholding, filtering, and region growing in solving the segmentation problem. Saha et al. (8) described a method using the multiscale morphologic signature of individual objects at conjoining locations that requires no previous knowledge of constraints on geometric, shape, or image intensity models for individual objects. This method uses the theory and algorithms similar to those implemented for solving the problem of segmenting and separating pulmonary arteries and veins through in vivo CT imaging with no contrast medium.

The HRES images cover a large volume and may contain multiple acini. To save processing time and memory resources, cropping to a smaller region of interest was required. Several preprocessing steps for the cropped dataset were performed before separation could be performed. An unsharp mask filter (implemented in FIJI; www.fiji.sc) was applied to enhance contrast. This filter allowed a more aggressive thresholding that eliminated most of the "salt and pepper" noise in air spaces (Fig. 1 *A* and *B*). After a threshold was chosen manually, a seed point was selected on the wall structure, and a connected component algorithm (part of FIJI; http://fiji.sc/Find_Connected_Regions) eliminated any structures not connected to the walls, under the assumption that all alveolar septa are interconnected such as in a complex web. The remaining binary image of the wall structure was inverted to obtain a binary mask of the air spaces. If necessary, 3D erosions and dilations were performed to smooth some of the masks. This smoothing proved useful in cases where many incorrect wall fusions were still present. Erosion helps separate such microfusions.

The separation of an individual acinus from neighboring air spaces required further user interaction. Manual seed points had to be set to perform a correct separation (Fig. 1*D*). The air mask and seed points were used as the input parameters of the separation algorithm implemented for this application (8). The resulting air mask consisted of three labels, with the interior of the acinus of interest with one label, the remaining air spaces with a second label, and the wall structure as background. If the user missed false connections and failed to set sufficient separators, then more seed points were set for a second run in combination with the resulting mask. For the second run, the exterior air spaces had to be deleted, and new seed points were required on the remaining acinar structure. Separating other individual components of the lung parenchyma was also possible using the multiscale topomorphologic opening approach, but this was not so for the morphometric assessment in the present study.

Inconsistent gray-level intensities within the wall structures was a persistent problem for this method and required manual correction of the segmentations. Common manual corrections were used to eliminate false connections between acinar air spaces or to add walls that were incomplete. These errors of the segmentations were not significant for the computation of the volume or surface area, because only a few pixels at a time were missing. The corrections can be performed in any advanced image-viewing program that permits visualization of an overlay and editing. A software package developed in our laboratories, the Pulmonary Analysis Software Suite (22), or ITK-Snap (www.itksnap.org) (9) was used for this purpose.

**Preparation of Silicon Rubber Casts for Microscopic Analysis.** The study was performed with young adult male BALB/C mice with a body mass of 33 g. Silicon rubber casts were prepared following the in situ casting procedure of Phalen et al. (23), as described in detail by Rodriguez et al. (3). Anesthesia was induced by an i.p. overdose of Nembutal. After the trachea was intubated, the lung was collapsed by diaphragm incisions. TLC was estimated by graded inflation to 30 cm $H_2O$, followed by ventilation with 100% $CO_2$. After total collapse, a degassed saline solution was instilled at a pressure of 20 cm $H_2O$. Thirty minutes later, the saline was drained, and silicon rubber (Silastic E with some silicon oil added) was slowly infused through an infusion syringe over 1.5–2 h to achieve a filling corresponding to 60–70% of TLC. After polymerization, tissue was dissolved in a NaOH solution.

The casts were microdissected under an operating stereomicroscope following the airways to the periphery out to TBs where the first alveolus appears on the airway wall, as described previously (2, 3). TBs were transected,

and the isolated acini were collected and weighed to estimate acinar volume. A systematic uniform random sample of these acini was then mounted on metal supports for scanning electron microscopy by means of cyonalite glue and gold coated by sputtering. Several additional lungs were fixed by vascular perfusion (24) while being inflated with air at approximately 60% of TLC for comparison with the casts.

**Morphometric Analysis of Acinar Composition.** The final segmentation of an acinus was used to compute the acinar volume by multiplying the number of voxels by the voxel size. All images were acquired with a linear resolution and slice thickness of 2 µm. The surface area resulted from summing all triangles generated by a marching cube algorithm used to create a surface mesh of the image mask (25). The surface was smoothed using a size-preserving algorithm (26).

To further describe the morphometry of the acinus, a method was implemented to estimate the number of alveoli in an acinus based on stereology (13, 27, 28) and applied to segmented images from micro-CT datasets. Estimation of alveolar number was done by application of the physical disector approach (27, 28). These disector slice pairs were systematically randomly chosen at random from within the stack according to the fractionator principle (28). Approximately 20 slice pairs were needed to obtain a total count of roughly 200 events, which has been shown to be sufficiently precise (27, 29). A section pair used for the disector was composed of a slice and the third consecutive slice forming a distance (disector height) of 6 µm between them. Counting was done by comparing the corresponding entire section pairs. For counting, the images were named in sequence and loaded in the online STEPanizer program (30). Results were exported to a spreadsheet (Microsoft Excel) after counting was completed.

Images with an overlaid outline of the segmentation were used. We use one of the datasets as an example to describe this procedure. This dataset had a total of 700 slices. After image segmentation, the images and corresponding mask were combined into one image, in which the mask was represented by a red line (Fig. 6). Only slices that contained the outlined acinus were included in the sampling procedure (670 slices in this example). The red line made it possible to perform the counting in only one acinar structure that was part of the segmented acinus. A counting event is defined as the presence of an alveolar opening in one slice of the disector pair but not in the other slice (termed a bridge; Fig. 6). The application of the acinar surface mask constitutes a layer applied to the septal surface, which thickens the structure by one voxel. This may cause a small degree of overestimation in the number of bridges. To ensure the validity of a counting event, the serial sections can be inspected without the outline at the location of an unclear bridge. Counting was performed in both directions, with each slice used once for counting and once for comparison. The total number of alveoli per acinus was determined according to the fractionator principle by multiplying the number of counted bridges by the inverse of the slice sampling fraction, which is the ratio of the disector height (6 µm) times the number of disectors sampled, divided by the total height of the acinus in the z-axis direction (i.e., the number of slices containing the acinus times the slice thickness of 2 µm).

The present micro-CT methods do not provide sufficient contrast to distinguish the fibers located at the alveolar entrance ring that are typically seen in microscopy and used to identify alveolar openings. Nonetheless, an alveolus can be readily identified by its shape and by the walls that form it. The advantage of a volumetric scan is that one can scroll through the stack and observe the course and integrity of septal walls. Thus, alveolar openings can be confirmed, whereas broken walls or pores of Kohn can be excluded from the counting by using the entire stack of images, not just the randomly selected disector slices.

1. McDonough JE, et al. (2011) Small-airway obstruction and emphysema in chronic obstructive pulmonary disease. *N Engl J Med* 365:1567–1575.
2. Haefeli-Bleuer B, Weibel ER (1988) Morphometry of the human pulmonary acinus. *Anat Rec* 220:401–414.
3. Rodriguez M, Bur S, Favre A, Weibel ER (1987) Pulmonary acinus: Geometry and morphometry of the peripheral airway system in rat and rabbit. *Am J Anat* 180:143–155.
4. Sapoval B, Filoche M, Weibel ER (2002) Smaller is better—but not too small: A physical scale for the design of the mammalian pulmonary acinus. *Proc Natl Acad Sci USA* 99:10411–10416.
5. Swan AJ, Tawhai MH (2011) Evidence for minimal oxygen heterogeneity in the healthy human pulmonary acinus. *J Appl Physiol* 110:528–537.
6. Mercer RR, Crapo JD (1987) Three-dimensional reconstruction of the rat acinus. *J Appl Physiol* 63:785–794.
7. Vasilescu DM, Knudsen L, Ochs M, Weibel ER, Hoffman EA (2012) Optimized murine lung preparation for detailed structural evaluation via micro–computed tomography. *J Appl Physiol* 112:159–166.
8. Saha PK, Gao Z, Alford SK, Sonka M, Hoffman EA (2010) Topomorphologic separation of fused isointensity objects via multiscale opening: Separating arteries and veins in 3-D pulmonary CT. *IEEE Trans Med Imaging* 29:840–851.
9. Yushkevich PA, et al. (2006) User-guided 3D active contour segmentation of anatomical structures: Significantly improved efficiency and reliability. *Neuroimage* 31:1116–1128.
10. Bachofen H, Wangensteen D, Weibel ER (1982) Surfaces and volumes of alveolar tissue under zone II and zone III conditions. *J Appl Physiol* 53:879–885.
11. Huang K, Rabold R, Schofield B, Mitzner W, Tankersley CG (2007) Age-dependent changes of airway and lung parenchyma in C57BL/6J mice. *J Appl Physiol* 102:200–206.
12. Ochs M (2006) A brief update on lung stereology. *J Microsc* 222:188–200.
13. Weibel ER (1963) *Morphometry of the Human Lung* (Academic, New York).
14. Phalen RF, Oldham MJ (1983) Tracheobronchial airway structure as revealed by casting techniques. *Am Rev Respir Dis* 128:S1–S4.
15. Kumar H, Tawhai MH, Hoffman EA, Lin CL (2011) Steady streaming: A key mixing mechanism in low-Reynolds number acinar flows. *Phys Fluids (1994)* 23:41902.
16. Lin CL, Tawhai MH, McLennan G, Hoffman EA (2007) Characteristics of the turbulent laryngeal jet and its effect on airflow in the human intra-thoracic airways. *Respir Physiol Neurobiol* 157:295–309.
17. Lin CL, Tawhai MH, McLennan G, Hoffman EA (2009) Computational fluid dynamics. *IEEE Eng Med Biol Mag* 28:25–33.
18. Yin Y, Choi J, Hoffman EA, Tawhai MH, Lin CL (2010) Simulation of pulmonary air flow with a subject-specific boundary condition. *J Biomech* 43:2159–2163.
19. Miyawaki S, Tawhai MH, Hoffman EA, Lin CL (2012) Effect of carrier gas properties on aerosol distribution in a CT-based human airway numerical model. *Ann Biomed Eng* 40:1495–1507.
20. Amy RW, Bowes D, Burri PH, Haines J, Thurlbeck WM (1977) Postnatal growth of the mouse lung. *J Anat* 124:131–151.
21. Thiesse J, et al. (2010) Lung structure phenotype variation in inbred mouse strains revealed through in vivo micro-CT imaging. *J Appl Physiol* 109:1960–1968.
22. Guo J, Fuld MK, Alford SK, Reinhardt JM, Hoffman EA (2008) Pulmonary Analysis Software Suite 9.0: Integrating quantitative measures of function with structural analyses. *Proceedings of the First International Workshop on Pulmonary Image Analysis*, eds Brown M, et al. (Lulu.com), pp 283–292.
23. Phalen RF, Yeh HC, Raabe OG, Velasquez DJ (1973) Casting the lungs in situ. *Anat Rec* 177:255–263.
24. Bachofen H, Ammann A, Wangensteen D, Weibel ER (1982) Perfusion fixation of lungs for structure-function analysis: Credits and limitations. *J Appl Physiol* 53:528–533.
25. Lorensen WE, Cline HE (1987) Marching cubes: A high-resolution 3D surface construction algorithm. *Comput Graph* 21:163.
26. Taubin G (1995) Curve and surface smoothing without shrinkage. *Proceedings Fifth International Conference on Computer Vision*, Cambridge MA, June 20-23, 1995 (IEEE, New York, NY).
27. Ochs M, et al. (2004) The number of alveoli in the human lung. *Am J Respir Crit Care Med* 169:120–124.
28. Hyde DM, Tyler NK, Putney LF, Singh P, Gundersen HJ (2004) Total number and mean size of alveoli in mammalian lung estimated using fractionator sampling and unbiased estimates of the Euler characteristic of alveolar openings. *Anat Rec A Discov Mol Cell Evol Biol* 277:216–226.
29. Gundersen HJ, Jensen EB, Kiêu K, Nielsen J (1999) The efficiency of systematic sampling in stereology—reconsidered. *J Microsc* 193:199–211.
30. Tschanz SA, Burri PH, Weibel ER (2011) A simple tool for stereological assessment of digital images: The STEPanizer. *J Microsc* 243:47–59.

www.manaraa.com